MAPPING OF SMALL-SCALE URBAN SCENES BY AIRBORNE MMW FMCW SAR ON CIRCULAR FLIGHT TRAJECTORIES

S. Palm[*][†]

[*] Technische Universität München, Photogrammetry and Remote Sensing, München, Germany
[†] Fraunhofer FHR, High Frequency Radar and Applications, Wachtberg, Germany

Abstract

The image-based acquisition of the current situation in urban areas is essential for various applications. In contrast to the typical SAR acquisition geometry from a single aspect on linear flight trajectories, this work considers mapping a small-scale area by data acquisition from various aspects on circular flight trajectories (CSAR). To meet the high requirements of aligning a narrow radar beam continuously to the point of interest during low-altitude circular flights, an automatic beam stabilization has been developed and operationally tested. A new and very broadband frequency-modulated SAR (FMCW) in the millimeter wave domain (mmW) at 94 GHz enables ultra-high-resolution imaging, and the compact design allows its operation on small aircraft. Dynamic visualization of the illuminated scene, similar to a video, is realized by a developed focusing method optimized for the unique acquisition geometry by processing overlapping subapertures (ViCSAR). 3d reconstruction of individual objects is achieved with single-channel data by extracting the movement of scattering centers on the SAR image sequences. To validate the CSAR methods, experimental measurement flights were carried out along circular flight trajectories with an ultralight aircraft (94 GHz FMCW SAR) over a suburban area. The results indicate that ultra-high-resolution SAR images with azimuth resolutions < 2 cm and 3D point clouds can be derived. Moving objects like vehicles are observable by their radar shadows in the coregistered and georeferenced image sequences. These methods can likely be used to derive radar signatures from buildings or ships and enable high-resolution SAR missions on unmanned platforms (UAVs).

Keywords

Remote Sensing; Airborne mmW FMCW SAR; Video Circular SAR; Steerable antennas, UAV

1. INTRODUCTION

The image-based acquisition of the current situation in urban areas is of great importance for various applications, including urban planning, environmental risk management, or mapping 3d city models. Due to the independence of weather and daylight conditions, SAR is particularly suitable for time-independent scene acquisition. In contrast to the typical SAR acquisition geometry from a fixed aspect angle operated on airborne or spaceborne linear flight trajectories, this paper considers mapping a small-scale area by a data acquisition on circular flight trajectories and, thus, varying aspect angles (CSAR). This acquisition geometry offers a large number of unique features for new imaging techniques [1,2]. Of particular interest is the capability of very high-resolution imaging [3] and 3d extraction that includes methods like operating on multi-circular apertures [4, 5], fully polarimetric 3d imaging [3], multi-pass circular holographic SAR tomography [6] or radargrammetic 3d extraction [7].

Mapping of urban scenes with data acquired on circular trajectories has received little attention so far, although multi-aspect InSAR data fusion with data acquired from multiple linear flight paths has shown great potential [8]. The application of mmW frequencies in the W-band offers new potential as the wavelength is by a factor of ten smaller than in previous experiments in X or even L-band. On the one hand, this allows very high-resolution imaging, and the wavelength may interact very beneficial with small-scale urban objects due to the different roughness characteristics. On the other hand, due to modern semiconductor technology, very compact and, therefore, lightweight mmW frequency modulated continuous wave (FMCW) radar systems can be designed at very high carrier frequencies. These SAR sensors allow the operation of small and cost-efficient platforms, like small aircraft or even drones.

Therefore, this research investigates and demonstrates for the first time a sensor concept capable of acquiring a $360°$ W-band full-aspect data set carried by a small aircraft in Section 2. It further presents a method to jointly visualize the $360°$ urban data set by a video-like representation and a method to extract 3d information in Section 3. Flight experiments are shown in Section 4, the results and discussion is presented in Section 5 and Section 6 concludes the paper.

2. BEAM STEERABLE SAR SENSOR DESIGN

2.1. Acquisition geometry

The typical acquisition geometry of a spaceborne or airborne SAR sensor is on a preferably linear trajectory at constant height h_z while illuminating the scene in a side-looking geometry with a depression or elevation angle ϵ or θ, respectively, as indicated in Fig. 1a. In this mode, the beam width of the radar in elevation ϱ is commonly chosen to be significantly larger than the beam width in azimuth β. Further, L_s indicates the size of a full synthetic aperture while L_x the size of a subaperture - a smaller portion of the full aperture.

In contrast, in CSAR, the sensor ideally follows a circular trajectory with a radius R_m as indicated in Fig. 1b. In this geometry, antennas with the same beam width in elevation and azimuth are beneficial since they allow the illumination of a large ground area over an angular aspect interval of $360°$. While the central area with size $\pi \cdot R_c^2$ is then illuminated in full-aspect mode, the outside area $\pi \cdot (R_i - R_c)^2$ is illuminated in a minor aspect interval. Objects in the center area that are visible over the entire aspect interval have a synthetic aperture length of $L_s = 2\pi \cdot R_m$ that allows very high-resolution processing. In theory, the resolution in CSAR can reach up to $\frac{\lambda}{4}$ instead of $L/2$ in stripmap mode on a linear trajectory with λ the emitted wavelength and L the length of the antenna [3].
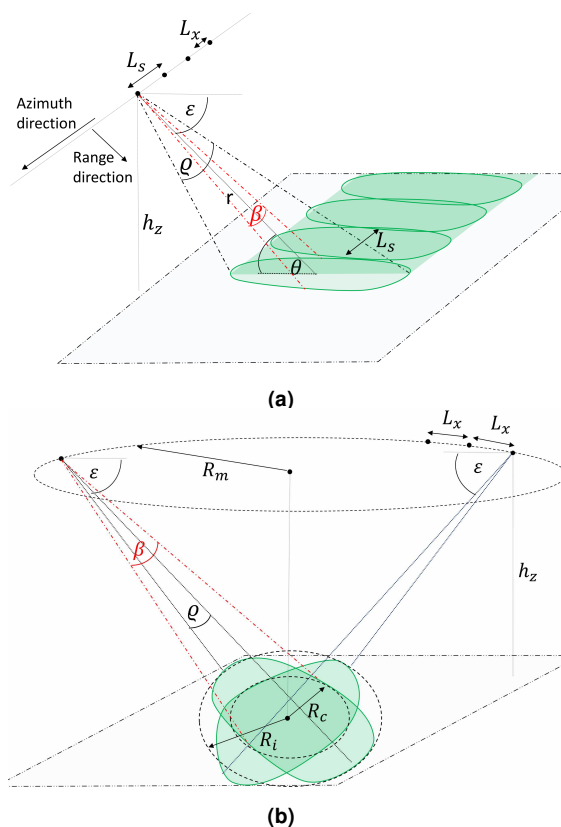

(a)

(b)

FIG 1. SAR acquisition geometry with indicated footprint. a) SAR on a linear trajectory (stripmap), b) SAR on a circular trajectory (CSAR).

2.2. Challenges acquiring mmW CSAR data

Acquiring a high resolution $360°$ data set with an airborne W-band SAR of a sufficiently large ground area places severe demands on both the sensor system and the operating pilot. Challenging are mainly four features that one would like to achieve with circular SAR data: (i) a permanently directed radar main lobe to the target center (point of interest), (ii) illumination of an ideally large surface area, (iii) transmission of high radio frequencies (RF) bandwidths B, and (iv) providing sufficient output power P_e according to the desired resolution.

One major limiting factor for realizing these features in this frequency domain is the low output power of broadband, high-performance, and semi-conductor-based W-band amplifiers. These are currently limited to 24-30 dBm [9], so airborne data collection must be performed at relatively low altitudes to achieve reasonable Signal-to-Noise-Ratios (SNR). Additionally, in order to restrict the amount of data due to PRF limits at high RF bandwidths and to focus the low output power, the antenna beam width ϱ and θ can not be chosen arbitrarily large.

Consequently, flying small radii at low altitudes with moderate speed is rather suitable for smaller aircraft or UAVs. However, these light platforms typically have low wing loading and are more sensitive to thermal lift or wind. Further, flying an exactly circular flight path over the ground at a low altitude while maintaining a predefined, constant roll angle and simultaneously aligning the radar beam to the point of interest places severe demands on the pilot's flight control. Deviation from the specified roll, pitch, or yaw angles can cause the footprint to leave the point of interest. This is further hindered by a constantly changing wind vector hitting the platform during circling (headwind, crosswind, tailwind).

Initiated corrective flight maneuvers by the pilot typically cause a roll or drift movement. As a result, the aircraft no longer moves tangentially along the circular path, causing the beam not to remain aligned with the target area. Even in the case of an ideal circular flight path, the radar antenna would have to be installed in the center of the rotation. However, this is generally not the case, e.g., when the sensor is suspended on the wing.

2.3. Real-time beam steering method

2.3.1. Requirements

Further flight control and beam stabilization specifications can be derived by evaluating the optimal flight height and the possible range of a high-performance W-band sensor in the circular acquisition geometry. This is realized by calculating the integrated backscattering energy of a potential object in relation to the required SNR of an image pixel. Given the radar equation from [10], the received power P_r of the radar is a
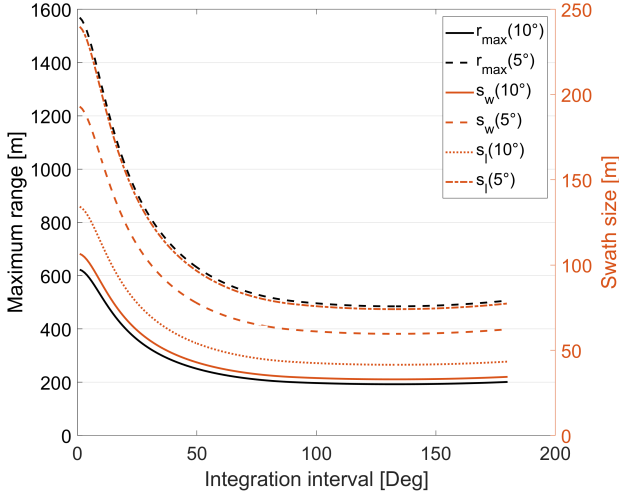
FIG 2. Achievable distances and swath sizes of a high performance W-band radar in CSAR mode as a function of the aspect integration interval φ_{az} and antenna beam width ($5°$ and $10°$). Simulated parameters are: $P_e = 29$ dBm, N=25 dB, θ=$35°$, B=2 GHz, v_s=35 m/s, σ_0=-10 dBm^2/m^2, λ=3.2 mm.

function of the emitted power P_e given by

$$(1) \qquad P_r = P_e \cdot \frac{G^2 \sigma \lambda^2}{4\pi^3 \cdot r^4}$$

while G is the antenna gain, σ the object's RCS and r the range or distance. With knowledge of $G = \frac{4\pi \cdot L}{\lambda \cdot \varrho}$, the RCS of each pixel $\sigma = \delta_x \cdot \delta_y \cdot \sigma_0$ and the collected energy $W_r = P_r \cdot T_s$ over the circular synthetic aperture, the maximum range r_{max} can be approximated by [11]

$$(2) \qquad r_{max} = \sqrt[3]{\frac{P_e \cdot L^2 \cdot \delta_y \cdot \delta_x \cdot \sigma_0 \cdot \cos(\theta) \cdot \varphi_{az}}{4\pi \cdot \varrho^2 \cdot \left|\vec{\mathbf{v}}_s\right| \cdot 10kT_K N}}.$$

$T_s = \frac{r \cdot \cos\theta \cdot \varphi_{az}}{\vec{\mathbf{v}}_s}$ specifies the integration time of the synthetic aperture, φ_{az} the integrated aspect angle, $\vec{\mathbf{v}}_s$ the platform velocity and δ_x, δ_y the processed range and azimuth resolution, respectively. To achieve good image contrast, it is further assumed that each image pixel should provide an SNR of at least 10 which results in $W_r = 10kT_K N$ with $k = 1.38 \cdot 10^{23} Ws/K$, T_K the temperature and N the radar's Noise number.

Fig. 2 evaluates r_{max} of a high-performance radar as a function of the processed resolution (integration interval) for grassland which typically has a RCS of -10 dBm^2/m^2. In addition, the size of the potential footprint on the ground (swath length s_l, swath width s_w) is indicated for two possible antenna beam widths. The results of Fig. 2 show that r_{max} for a $10°$ antenna beam width is limited to 500-600 m corresponding to a flight height of about 300 m. This allows swath sizes of about 100-130 m and coherent integration intervals φ_{az} of one up to several degrees corresponding to processed azimuth resolutions δ_y of about 1 cm up to 15 cm. The achievable resolu-

tion increases rapidly with small φ_{az}, therefore, the resolution cells become smaller and r_{max}, given the same SNR, decreases significantly. Although a $5°$ antenna beam width increases the range, it places significantly more demands on the beam correction. Experimental studies carried out on an ultralight aircraft, see Fig. 4a, at the derived flight height indicate that the standard deviations of flight parameters such as roll or squint angles, or the absolute velocity within a synthetic aperture are 40% higher on circular than on linear flight paths [11]. Further, it was not even possible for an experienced pilot who was trained in flying circular trajectories to continuously align the radar footprint on the center of the circle. The experiments showed that a correction rate of approximately $12°$ in roll, $8°$ for pitch, and $10°$ for heading with angular velocities of up to $6°/s$ was required to stabilize the radar beam [11].

2.3.2. Realized implementation

For the automatic antenna beam steering, a gyro-stabilized mount CSM 130 from Somag was acquired, and the miniaturized radar front-end was integrated into it. The mount is designed by the manufacturer to typically hold a camera in the nadir position and automatically compensate for changes in position or angle. For automatically align the sensor to a programmable GPS coordinate as the point of interest in CSAR mode, a real-time framework has been designed and implemented in cooperation with IGI mbH. The realized framework consists of a programmable interface between GPS/INS, real-time processing hardware, and the stabilized mount and is indicated in Fig. 3.

Any change in the mount's attitude angle is recorded by the FOG IMU, which is positioned on top of the rotatable mount elements. The real-time GPS/INS data packages are continuously transmitted via TCP/IP at a data rate of 128-512 Hz to an onboard processor that calculates the actual footprint position and required angular correction to the point of interest. The derived solution for realigning the mount's angular position is converted into control commands and sent via a second TCP/IP link to the mount and executed. Thus, the sensor system represents a closed loop and automatically aligns the beam to the point of interest. Required input parameters are the GPS coordinate and height of the point of interest and the beam alignment update rate, which is typically 4 Hz. Further details on deriving the optimal angular solutions in real-time are presented in [11].

2.4. SAR sensor integration

The MIRANDA-94 W-band radar integrated into the gyro stabilized mount is a compact and lightweight FMCW airborne SAR operating at 94 GHz and presented in Fig. 4a. With an output power of P_e=29 dBm, it can generate up to B=10 GHz RF bandwidth and is designed and operated at Fraunhofer FHR. Essential components like frequency multiplier, mixer, low
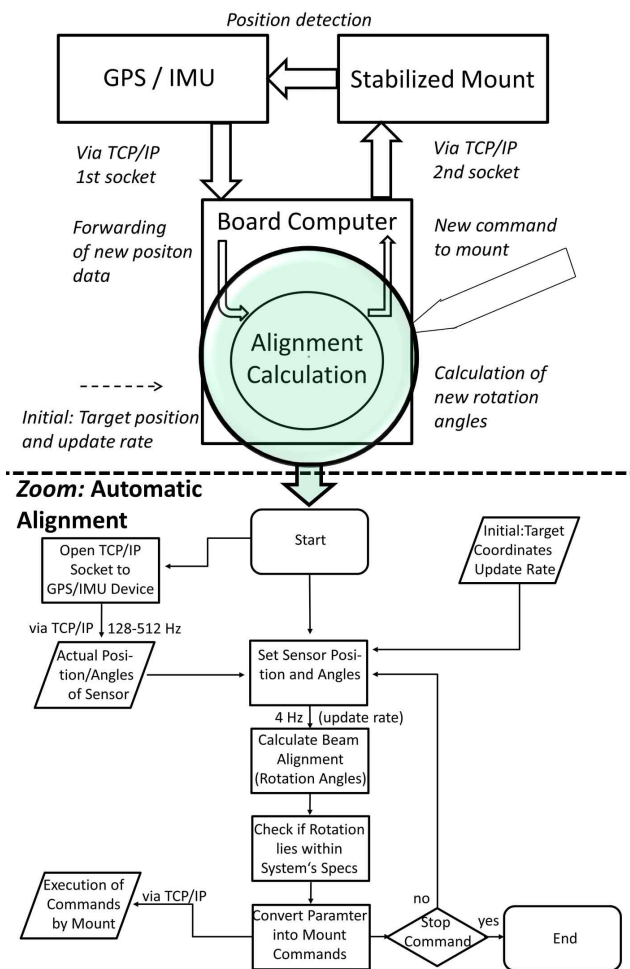
FIG 3. Real-time beam steering design. Top) Data flow between GPS/IMU, processor and mount, Down) Flow chart of real-time software interface for automatic beam alignment.

FIG 4. Beam-stabilized W-band SAR installed on aircraft wing and in the lab. a) Ultralight aircraft with CSAR sensor pot, b) Sensor in the lab. (A) IMU control unit, (B) radar back-end, (C) Onboard processor, (D) Stabilized mount, (E) steerable antennas, (F) FOG IMU.

Parameter	Description
Transmit power	29 dBm FMCW
Center frequency	94 GHz
RF bandwidth	up to 10 GHz
	CSAR 2 GHz
Resolution	< 2 cm
PRF	10 kHz
Total weight	25 kg
FOG GPS/INS	IGI (2.4 kg)
Mount (gimbal)	Somag CSM130
Mount steering rate	$15°/\sec$
Steerable angles	Roll/Pitch $\pm15°$,
	Heading $\pm25°$

TAB 1. MIRANDA-94 SAR sensor parameters [11, 13].

noise or high power amplifier are based on gallium arsenid technology and designed at Fraunhofer IAF [12]. The semi-conductor-based FMCW sensor allows a miniaturized and lightweight SAR system design with low input power, capable of being installed on small aircraft or UAVs. Further, the high transmission frequency in W-band enables the use of small antennas and the transmission of very high RF bandwidths that generate ultra-high resolutions.

The radar front-end with one transmit and two receive antennas are embedded in the stabilized mount, which allows a beam stabilizing for various acquisition geometries, including circular, spotlight, and stripmap SAR. Different antennas are operated depending on the acquisition geometry, while $10°$ horn antennas are used in CSAR mode. The miniaturized sensor weighs 25 kg (front-end weight is 2.5 kg) and is installed beneath the wing of an ultralight aircraft as presented in Fig. 4b. A precise FOG GPS/IMU, including dGPS processing, is operated to achieve extremely high resolutions at the very small wavelength. The system's specifications are shown in Table 1.

3. MAPPING OF URBAN SCENES WITH CSAR

The following chapter deals with the question of how the mmW circular acquisition geometry can enhance the mapping of urban scenes. First, a method is presented to jointly represent and visualize the $360°$ full-aspect data set in Section 3.1. Second, a method is shortly introduced to extract 3d information of individual objects by single-channel data processing in Section 3.2.

3.1. Subaperture circular SAR processing

One of the major benefits of W-band SAR imaging is the obtainable high azimuth resolution by coherently processing only a very small aspect interval φ_{az}, e.g. φ_{az} of $0.8°$ already results in δ_y=11 cm. In other words, the aircraft must move only a very short distance in a fraction of a second to acquire high-resolution SAR data. While the radar's spot is permanently directed to the same area in CSAR mode, this very short 'illumination time' per image can be used to generate a continuous stream of images similar to a video SAR (ViSAR) by subaperture processing. While the concept of ViSAR was proposed by Sandia National Laboratories for linear acquisition campaigns [14], the same urban scene content can continuously be processed from a slightly different aspect by operating on circular trajectories (ViCSAR). In the proposed ViCSAR mode, the $360°$ data set is processed using subapertures with equidistant step sizes of $\varphi_{az} = \varphi_{max}$ as indicated in Fig. 5a. The subaperture images at aspect φ are processed on a flat plane model with $E = (\mathbf{x} - (0,0,H_0)') \cdot \vec{\mathbf{n}}$ with $\vec{\mathbf{n}} = (0,0,1)'$ and H_0 the reference height as presented in Fig. 5a. The current position of the sensor at slow Time T at each subaperture is denoted by $\vec{\mathbf{x}}_s(T)$ and starts with $\vec{\mathbf{x}}_{s0} = (0,0,h_z(T=0))$. φ_{max} indicates the maximum aspect integration interval up to which objects with a specific height dh above/below the flat imaging plane can still be coherently focused, see [11]. The SAR processing is realized with a time-domain backprojection approach implemented highly parallel on multiple graphic cards in CUDA [11, 15]. As backprojection focuses the data in the aircraft's GPS/INS reference system, the images are geocoded in WGS84.

Image registration is performed by assigning the first subaperture image with fixed pixel spacing δ_p as the 'master image'. As the (n+1)-th image is processed in the same 'master image' geometry, the size of the (n+1)-th image plane ranging from $(x_{min}, ..., x_{max}; y_{min}, ..., y_{max})$ can be adapted in integer multiples of $u \cdot \delta_p$, $u \in \mathbb{N}$ depending on the footprint size, see Fig. 5b. This guarantees that no interpolation is required by fusing the individual images to a 3d image stack. By this method, the aspect-dependent backscattering σ and phase information ϕ for an individual object placed at the reference height at $\vec{\mathbf{x}}_p$ is mapped into a single pixel column with

(3) $\qquad \vec{\mathbf{x}}_p \rightarrow (\vec{x}_p, \sigma_{1,...,n}, \phi_{1,...,n}, \varphi_{1,...,n}).$

A further increase in the frame rate of the geocoded image sequence can be achieved by processing the subapertures with high overlap factors, typically between 60-80% [11]. The spectral information of the (n+1)-th subaperture then comprises a high overlap of the n-th subaperture. This further affects a 'more smooth' visualization of urban scenes since scatterers above the imaging plane show an arc-like movement caused by the projection geometry. This movement

otherwise can easily reach several pixels from image to image at high resolution and hinders the detection of dynamic events in the scene.
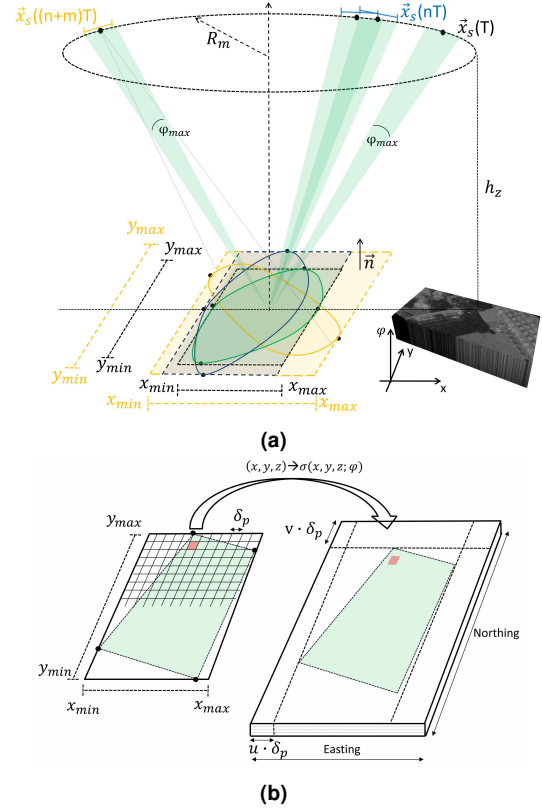

(a)

(b)

FIG 5. CSAR subaperture and 3d image stack processing. a) Images from various aspects focused in the same image geometry, b) registration of geocoded SAR images in a 3d image stack.

3.2. Extraction of 3d point clouds

If scattering centers are at a height dh above/below the reference plane, they can only be processed coherently up to a maximum angular interval $\varphi_{max}(dh)$ that is further derived in [13]. Applying processing intervals larger than $\varphi_{max}(dh)$ results in a process that the target's energy is smeared along multiple resolution cells. The proposed method locally evaluates this energy flow in search matrices $x_l(H_i, \varphi)$ while the full-aspect SAR data is first divided in equidistant arcs and then focused at different reference heights $H_i, i \in \mathbb{N}$ with $\varphi_{az} \gg \varphi_{max}$ as indicated in Fig. 6. Two normalized metrics $\vec{s}_n(H)$ were designed to determine the local energy flow by analyzing the pixel distribution and the spectral components of $x_l(H_i, \varphi)$. The local 3d information $\vec{\mathbf{x}}_p$ can then be extracted by the normalized operator's maximum given by

(4) $\qquad \vec{\mathbf{x}}_p = g\left(arg\left[\max_H\left(\frac{\vec{s}_n(H)}{\sum \vec{s}_n(H)}\right)\right]\right).$

A final step fuses the locally derived 3d point clouds from the equidistant arcs to a global 3d point cloud. For a more detailed presentation, the reader is referred to [11, 16].
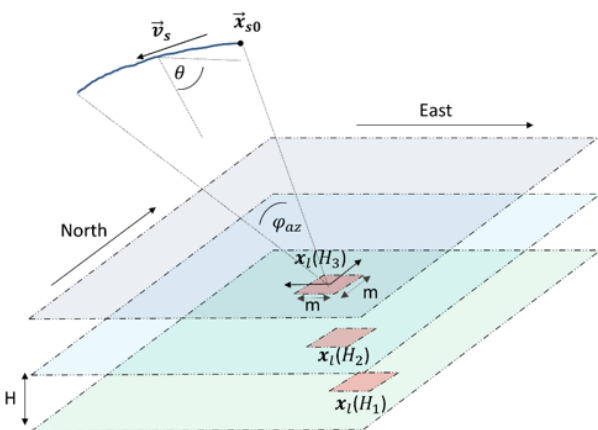
FIG 6. Corresponding search matrices $x_l(H_i, \varphi)$ in an image stack focused at different reference heights from a single aspect.

4. EXPERIMENTS

Flight campaigns on circular trajectories were performed with the MIRANDA W-band sensor installed on the ultralight aircraft DELPHIN as presented in Fig. 4b. Fig. 7 shows the acquisition campaign over a commercial shopping area in Berkum, Germany, with several large buildings, a parking space, trees, and a fuel station. While the center of the red trajectory was over the largest shopping building, the green one was over an adjacent roundabout traffic. The flight height was 300 m AGL while the radius R_m was 360 m.

FIG 7. CSAR flight campaign over an urban scene and a roundabout. The illuminated area is highlighted.

While acquiring the data set, the SAR sensor is remotely operated from a ground-station team which typically consists of two persons, see Fig. 8. A remote data link to the aircraft can operate up to 40 km and is used to monitor the sensor parameters, start/stop the beam steering mode, or data storage. In addition, a real-time SAR image stream with minor resolution processed onboard the aircraft is transmitted via the data link. More details about the processing architecture are shown in [17].
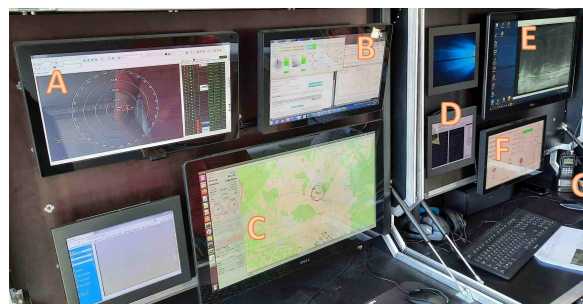

FIG 8. Ground station operation screens. (A) Mode-S, (B) telemetry, (C) flight path, (D) mount control, (E) real-time SAR, (F) data storage, (G) radio.
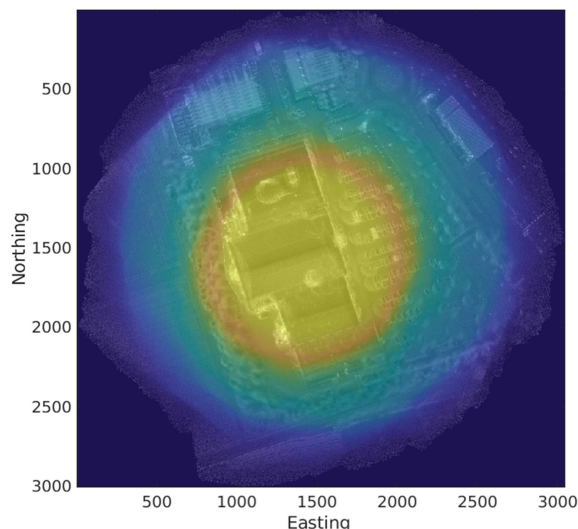

FIG 9. Full-aspect $360°$ multilook SAR image with superimposed color-coded heatmap indicating the radar's footprint at the circular acquisition.

5. RESULTS AND DISCUSSION

5.1. Mechanical beam steering results

A qualitative analysis of the implemented beam steering method results is presented in Fig. 9. The Figure shows a $360°$ CSAR image of the urban scene (red flight Fig. 7) composed of more than 800 geocoded subaperture SAR images at slightly varying aspects non-coherently summed up. Thus, each pixel indicates the mean absolute backscattering from the total $360°$ data set. Transparently overlaid and color-coded is a geocoded heatmap in the same image geometry indicating for each pixel how often it is located in the 3 dB main lobe of the radar beam. It is observable from the results that the point of interest in this data acquisition was the largest commercial building with its main entrance. Despite the challenging flight geometry, the radar beam remains fixed to the center of the target, which enables the acquisition of a full-aspect data set even on small radii.

The footprint size is sufficient for mapping small urban areas like individual buildings, parking areas, fuel stations, or road crossings and roundabouts. With increased output powers in the future, the aircraft can
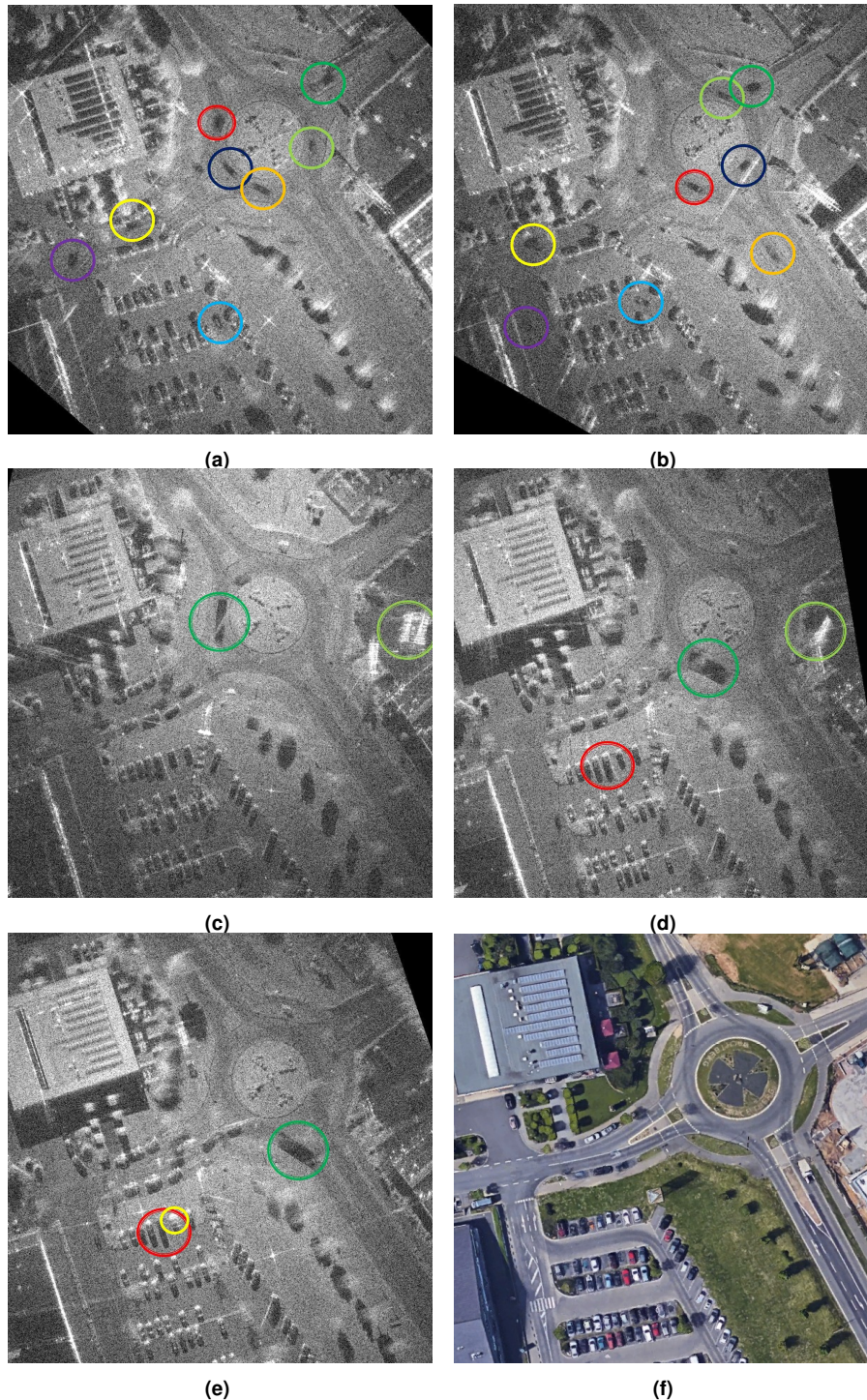
FIG 10. ViCSAR results of roundabout area with 7.5 cm resolution. The moving shadows of several cars and a bus at moderate speed are color highlighted. Illumination time is 0.35 sec for each image. Acquisition time T: (a) T=0 sec, (b) T=2.8 sec, (c) T=21 sec, (d) T=22.3 sec, (e) T=23.7 sec, (f) aerial photo (Google).

fly higher, and the footprint can be considerably increased. Besides the CSAR mode, the stabilized system has recently also been successfully applied in an airborne E-band communication data link experiment from aircraft to the ground station with significantly smaller antenna beam widths [18].

5.2. ViCSAR imaging results

Results for the ViCSAR imaging are shown in Fig. 10 presenting the area of the parking space (southwest),

the fuel station (northwest) and the roundabout (northeast) at subsequent times acquired by the green trajectory from Fig. 7. A part of the entire video sequence can be watched online following the link in [19]. The processed resolution in range and azimuth is 7.5 cm. As the corresponding illumination time for each subaperture is only very short with 0.35 sec, the visualization of dynamic events in the scene is possible. The moving shadows of several vehicles in Fig. 10a and Fig. 10b are color highlighted
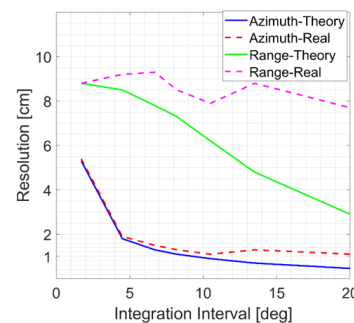
7
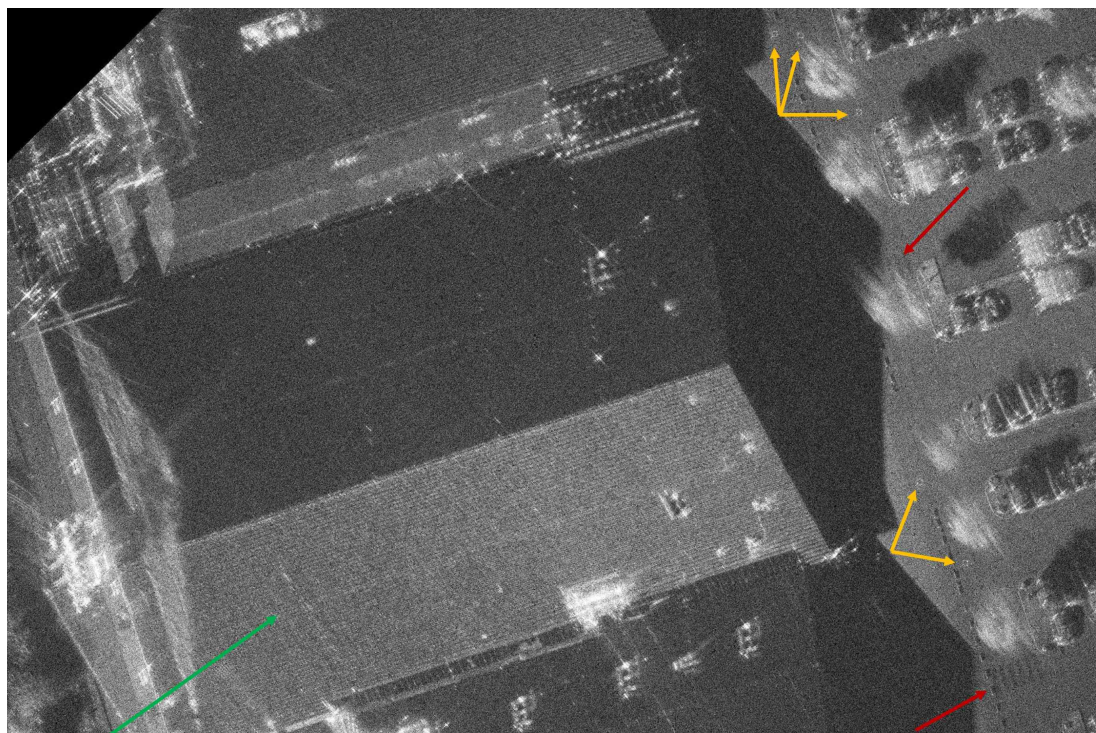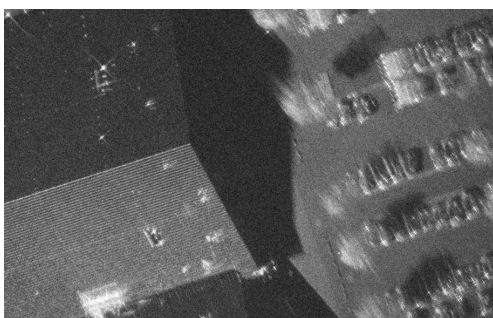
FIG 11. Very high-resolution subaperture SAR image of central building of urban area. a) Focused at street level height with $\varphi_{az} = 8.5°$. Gully covers are indicated by an orange, street crossings by a red and radar's line of sight by a green arrow, b) area focused at 10 m above the street level, c) enlarged street crossing in front of the central building from a different aspect. d) measured resolution of a reflector as a function of φ_{az}.

to visualize better the potential of tracking such objects in subsequent images. Due to the processed overlap factor, consecutive images have a time distance of about 0.1 sec. The time lag between Figures (a) and (b) is approximately 2.8 sec.

In Fig. 10c to Fig. 10e, a bus (dark green) is driving in the roundabout and finally leaves it in the southern direction. The defocused and displaced signature of the moving bus is marked in light green and is better or less recognizable depending on the actual doppler offset and aspect angle. Further, in Fig. 10e and 10f, a parked car is being monitored in the process of driving away (red circle and yellow doppler signature offset). The ability to detect and monitor dynamic events in an urban scene, e.g., by tracking moving shadows of moving vehicles in consecutive image frames, even in single-channel CSAR data, is demonstrated. Moreover, as the urban scene is continuously illuminated, it can be observed in which direction, e.g., a car is

leaving the roundabout or parking area. Further, due to the small aperture length, an observer may usually find an optimal aspect angle even to image smaller objects with low angular visibility that may be hidden from prominent buildings.

Benefit also comes from a different physical property of mmW, which is the diffuse scattering of relatively smooth surfaces. In W-band, the asphalt of, e.g., streets is significantly rougher than in X-band SAR. Thus, a potential moving shadow shows much more contrast. The small wavelength is also more sensitive to small-scale objects in urban scenes like, e.g., roof tiles, street lamps, or leaves.

5.3. Very high-resolution CSAR imaging

Results for mapping the urban scene in very high resolution by processing large aspect intervals of $\varphi_{az} = 8.5°$ are presented in Fig. 11. The Figure shows the central building and parts of the parking space. Ob-

jects located at the derived reference height show azimuth resolutions < 2 cm while the range resolution is still limited to the emitted RF bandwidth corresponding to 7.5 cm. In combination with the small wavelength, this enables the detection of fine-scale objects such as gully covers (marked orange) or street lamps, see Fig. 11a. Even crosswalks on the street (marked red) become observable since the surface of the road marking is much smoother than the asphalt, see Fig. 11c.

The height sensitivity in this acquisition geometry when processing such large intervals φ_{az} is further demonstrated in Fig. 11b. In comparison to Fig. 11a, the reference height of the focusing plane is not chosen to be at street level, instead, it is determined to be 10 m above this level. As a result, the top of the roof area, which has been rather defocused in Fig. 11a becomes sharply focused while street-level objects are smeared.

Analysis of the maximum spatial resolution that can be obtained by processing even larger φ_{az} is presented in Fig. 11d. For an aspect interval of $\varphi_{az} \in \{1°, .., 20°\}$ the achieved resolution of a corner reflector placed in the scene was measured and compared with the theoretically expected resolution.

The results indicate that azimuth resolutions of < 2 cm can be demonstrated for the circular acquisition geometry. However, from an integration interval of approx. $10°$, there is no longer any measurable increase in resolution. This suggests that the coherence at this limit likely is lost. Additionally, it would also explain why the range resolution can hardly be increased, since it is only significantly improved over a larger φ_{az}.

5.4. Extraction of 3d point clouds

Utilizing the effect of the height sensitivity by analyzing the energy flow of scattering centers focused at different reference heights as proposed in Section 3.2, the extraction of 3d information with single-channel data is possible. The result of a reconstructed $360°$ 3d point cloud by the proposed method is presented in Fig. 12. The Figure shows the commercial area with the main building in the center from a southeastern perspective. The quality of the 3d extraction of an area thereby depends primarily on the geometry of the object, its backscattering characteristic, and the material properties.

Obviously, large roof areas covered with roof tiles can be reconstructed well preserved while flat roofs hardly. This characteristic is due to the fact that roof tiles typically show a more point-like backscattering at least from a minor aspect while flat roofs in this data set consist of material that shows more clutter behavior. Similar noisy results are also for other clutter or volume scatterer regions like areas covered with streets or trees. Of course, the density of the point cloud also depends on the length of visibility of an object. As a result, the roof of the central building is best reconstructed. Still, peripheral areas that are only visible over a small angular interval can also be
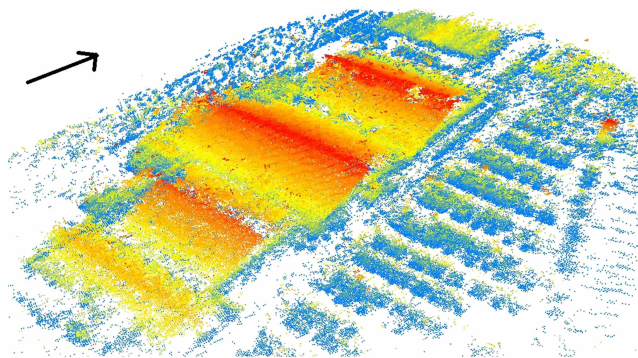

FIG 12. Computed 3d point cloud of the urban scene, from [16]. The arrow indicates north.

reconstructed with minor accuracy, depending on the object's characteristics. More details on the 3d point cloud reconstruction's qualitative and quantitative analysis are given in [11, 16].

6. CONCLUSION

During the course of this research, the first W-band FMCW SAR sensor explicitly designed for acquiring SAR data on circular trajectories has been demonstrated. Due to the ability to automatically steer the radar beam, it can be stated that the operation of such a sensor concept on a small aircraft and the various processing methods can provide valuable information about a small-scale urban area. The CSAR acquisition geometry and ViCSAR processing are particularly suited for mapping and monitoring urban scenes since the same area can continuously be observed for a longer time interval revealing dynamic events. Moving vehicles on streets and even pedestrians at favorable clutter backgrounds can be visualized and monitored by their moving shadows. The fact that asphalt shows rough surface characteristics in W-band is beneficial for single-channel moving target visualization.

Thus, W-band ViCSAR may certainly be beneficial in time-critical information acquisition like surveillance or disaster management applications. Further, the acquired full-aspect data can be imaged in ultra-high resolution (<2 cm), and 3d information of individual objects can be obtained.

In the future, these methods will probably open up the derivation of radar signatures of larger objects like buildings or ships and high-resolution imaging radar missions on unmanned platforms (UAVs). However, the accuracy of a 3d point cloud derived today by laser scanners can probably only be achieved with major difficulty in single-channel CSAR mode. A further disadvantage, at least at present, is the low output power of the W-band system that limits the flight altitude and spotlighted area.

Contact address:

stephan.palm@fhr.fraunhofer.de

References

[1] H. Cantalloube and E. Colin. Airborne SAR imaging along a circular trajectory. In *6th. European Conference on Synthetic Aperture Radar, EUSAR 2006*, pages 16–18, 2006.

[2] Alberto Moreira, Pau Prats-Iraola, Marwan Younis, Gerhard Krieger, Irena Hajnsek, and Konstantinos Papathanassiou. A tutorial on synthetic aperture radar. *IEEE Geoscience and Remote Sensing Magazine (GRSM)*, 1(1):6–43, März 2013.

[3] O. Ponce, P. Prats-Iraola, M. Pinheiro, M. Rodriguez-Cassola, R. Scheiber, A. Reigber, and A. Moreira. Fully polarimetric high-resolution 3-D imaging with circular SAR at L-Band. *IEEE Transactions on Geoscience and Remote Sensing*, 52(6):3074–3090, June 2014. DOI: 10.1109/TGRS.2013.2269194.

[4] S. Zhu, Z. Zhang, B. Liu, and W. Yu. Three-dimensional high resolution imaging method of multi-pass circular SAR based on joint sparse model. In *11th European Conference on Synthetic Aperture Radar, EUSAR 2016*, pages 1–5, June 2016.

[5] T. M. Marston and J. L. Kennedy. Volumetric acoustic imaging via circular multi-pass aperture synthesis. *IEEE Journal of Oceanic Engineering*, 41(4):852–867, Oct 2016. DOI: 10.1109/JOE.2015.2502664.

[6] O. Ponce, P. Prats-Iraola, R. Scheiber, A. Reigber, and A. Moreira. First airborne demonstration of holographic SAR tomography with fully polarimetric multicircular acquisitions at L-Band. *IEEE Transactions on Geoscience and Remote Sensing*, 54(10):6170–6196, Oct 2016. DOI: 10.1109/TGRS.2016.2582959.

[7] S. Palm, H.M. Oriot, and H.M. Cantalloube. Radargrammetric DEM extraction over urban area using circular SAR imagery. *IEEE Transactions on Geoscience and Remote Sensing*, 50(11):4720–4725, 2012. DOI: 10.1109/TGRS.2012.2191414.

[8] M. Schmitt and Uwe Stilla. Maximum-likelihood estimation for multi-aspect multi-baseline SAR interferometry of urban areas. *ISPRS Journal of Photogrammetry and Remote Sensing*, 87:68–77, 2014.

[9] Fabian Thome, Arnulf Leuther, Michael Schlechtweg, and Oliver Ambacher. Broadband high-power W-band amplifier MMICs based on stacked-HEMT unit cells. *IEEE Transactions on Microwave Theory and Techniques*, 66(3):1312–1318, 2018. DOI: 10.1109/TMTT.2017.2772809.

[10] I. G. Cumming and Frank H. Wong. *Digital processing of synthetic aperture radar data: Algorithms and implementation*. Artech House Inc., Boston, 2005.

[11] Stephan M. Palm. *Mapping of urban scenes by single-channel mmW FMCW SAR on circular flight and curved car trajectories*. Phd thesis, Technische Universität München, München, 2021.

[12] E. Ture, P. Brückner, M. Alsharef, R. Granzner, F. Schwierz, R. Quay, and O. Ambacher. First demonstration of W-band Tri-gate GaN-HEMT power amplifier MMIC with 30 dBm output power. In *IEEE MTT-S International Microwave Symposium, IMS 2017*, pages 35–37, June 2017.

[13] S. Palm, R. Sommer, D. Janssen, A. Tessmann, and U. Stilla. Airborne circular W-band SAR for multiple aspect urban site monitoring. *IEEE Transactions on Geoscience and Remote Sensing*, 57(9):6996–7016, Sep. 2019. DOI: 10.1109/TGRS.2019.2909949.

[14] L. Wells, K. Sorensen, A. Doerry, and B. Remund. Developments in SAR and IFSAR systems and technologies at sandia national laboratories. In *IEEE Aerospace Conference Proceedings*, volume 2, pages 1085–1095, 2003.

[15] A. Ribalta. Time-domain reconstruction algorithms for FMCW-SAR. *IEEE Geoscience and Remote Sensing Letters*, 8(3):396–400, 2011.

[16] Stephan Palm and Uwe Stilla. 3-d point cloud generation from airborne single-pass and single-channel circular sar data. *IEEE Transactions on Geoscience and Remote Sensing*, pages 1–20, 2020. In Press, doi=10.1109/TGRS.2020.3041320. DOI: 10.1109/TGRS.2020.3041320.

[17] Stephan Palm, Alfred Wahlen, Stephan Stanko, Nils Pohl, Peter Wellig, and Uwe Stilla. Real-time onboard processing and ground based monitoring of FMCW-SAR videos. In *10th European Conference on Synthetic Aperture Radar, EUSAR 2014*, pages 1–4, June 2014.

[18] I. Kallfass, R. Henneberger, R. Sommer, P. Harati, S. M. Dilek, B. Schoch, J. Eisenbeis, S. Marahrens, S. Palm, and A. Tessmann. High system gain e-band link in a wideband aircraft-to-ground data transmission. In *IEEE International Conference on Microwaves, Antennas, Communications and Electronic Systems, COMCAS 2019*, pages 1–5, 2019.

[19] Photogrammetry and Remote Sensing - TUM. *Airborne circular W-band SAR - Test area WachtbergKreisel [Video]*, May 2020. [Online]. Available: https://www.youtube.com/watch?v=cwDjJqtx_og and https://www.youtube.com/watch?v=D59hBaNwJXE.